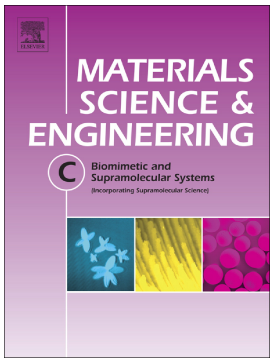


# Surface functionalization of cuttlefish bone-derived biphasic calcium phosphate scaffolds with polymeric coatings

Ana S. Neto, Ana C. Fonseca, J.C.C. Abrantes, Jorge F.J. Coelho, José M.F. Ferreira

PII: S0928-4931(19)31227-5

DOI: https://doi.org/10.1016/j.msec.2019.110014

Reference: MSC 110014

To appear in: *Materials Science & Engineering C*

Received date: 1 April 2019

Revised date: 4 July 2019

Accepted date: 25 July 2019

Please cite this article as: A.S. Neto, A.C. Fonseca, J.C.C. Abrantes, et al., Surface functionalization of cuttlefish bone-derived biphasic calcium phosphate scaffolds with polymeric coatings, *Materials Science & Engineering C* (2019), https://doi.org/10.1016/j.msec.2019.110014

# Surface functionalization of cuttlefish bone-derived biphasic calcium phosphate scaffolds with polymeric coatings

Ana S. Neto[1], Ana C. Fonseca[2], J.C.C. Abrantes[1,3], Jorge F. J. Coelho[2], José M.F. Ferreira[1*]

[1] *Department of Materials and Ceramic Engineering / CICECO – Aveiro Institute of Materials, University of Aveiro, 3810-193 Aveiro, Portugal*

[2] *CEMMPRE, Department of Chemical Engineering, University of Coimbra, Rua Sílvio Lima-Pólo II, 3030-790 Coimbra, Portugal*

[3] *UIDM, ESTG, Polytechnique Institute of Viana do Castelo, 4900 Viana do Castelo, Portugal*

* Corresponding author:
jmf@ua.pt;
Department of Materials and Ceramics Engineering, CICECO
University of Aveiro, Campus Santiago, 3810-193 Aveiro, Portugal
Tel: (+351) 234 370 242; Fax: (+351) 234 370 204

## Abstract

Cuttlefish bone (CB) has been explored as biomaterial in the bone tissue-engineering field due to its unique porous structure and capacity of the aragonite mineral to be hydrothermally converted into calcium phosphates (CaPs). In the present study, undoped and ion ($Sr^{2+}$, $Mg^{2+}$ and/or $Zn^{2+}$) doped biphasic calcium phosphate (BCP) scaffolds were prepared by hydrothermal transformation (HT, 200 ºC, 24 h) of CB. The obtained scaffolds were sintered and then coated with two commercial polymers, poly(ε-caprolactone) (PCL) or poly(DL-lactide) (PDLA), and with two synthesized ones, a poly(ester amide) (PEA) or a poly(ester urea) (PEU) in order to improve their compressive strength. The scaffolds were characterized by X-ray diffraction (XRD) coupled with structural Rietveld refinement, Fourier transform infrared (FTIR) spectroscopy, and scanning electron microscopy (SEM). The results demonstrate that CB could be entirely transformed into BCPs in the presence or absence of doping elements. The initial CB structure was preserved and the polymeric coatings did not jeopardize the interconnected porous structure. Furthermore, the polymeric coatings enhanced the compressive strength of the scaffolds. The *in vitro* bio-mineralization upon immersing the scaffolds into simulated body fluid (SBF) demonstrated the formation of bone-like apatite surface layers in both uncoated and coated scaffolds. Overall, the produced scaffolds exhibit promising properties for bone tissue engineering applications.


*Keywords*: Cuttlefish bone; Hydrothermal transformation; Biphasic calcium phosphate; Ion doping; Polymeric coatings.

## 1. Introduction

Bone is the second most transplanted tissue worldwide. Autografts, still considered the gold standard due to their optimal osteogenic, osteoinductive and osteoconductive properties, have multiple drawbacks, including the donor site morbidity and their limited availability [1]. In the last decades, bone tissue engineering has been regarded as a promising alternative to the current bone grafting approaches. It involves the use of porous 3D scaffolds that provide a suitable environment and architecture during bone regeneration and development [2].

Calcium phosphates (CaPs) are some of the most used materials for bone graft strategies due to their close resemblance with the mineral component of the bone [3]. Nowadays, biphasic calcium phosphates (BCP) are regarded with much interest [4,5]. Being a combination of a more stable phase, hydroxyapatite (HA), and a more soluble one, β-tricalcium phosphate (β-TCP), BCP biomaterials are often preferred for bone remodeling processes for enabling tailoring an adequate equilibrium between resorption/solubilization [6,7]. Certain ions existing in bone composition, such as strontium ($Sr^{2+}$), magnesium ($Mg^{2+}$) and zinc ($Zn^{2+}$) can be incorporated into the crystalline structure of CaPs in single or combined ways and might favorably influence their biological behaviors upon implantation [8]. $Sr^{2+}$ is present in bone in considerable quantities, mainly at regions with high levels of metabolic turnover. It enhances bone formation while depressing bone resorption by inducing the proliferation of pre-osteoblasts and its differentiation and increasing the apoptosis of osteoclast [9,10]. On the other hand, $Mg^{2+}$ is intimately related to the mineralization of the calcified tissues. Furthermore, $Mg^{2+}$ influences osteoblast and osteoclast activity and, thereby, the bone metabolism and bone growth [9,10]. $Zn^{2+}$ plays an important role in bone development and growth [9,10]. In addition, $Zn^{2+}$ is a trace element recognized for its antioxidant

and anti-inflammatory properties, with beneficial therapeutic effects in different diseases like atherosclerosis, neurodegeneration, immunologic disorders and cancer [11].

Despite all the above mentioned advantages, CaP materials are associated with poor mechanical properties (brittleness, fracture strength) thereby, limiting their use under load-bearing applications [3,12]. Bone is a typical natural composite, combining CaPs and natural polymers [13,14]. As matrices for engineered composites, synthetic polymers offer several advantages in comparison to natural polymers, since their properties can be tailored and their mechanical properties and degradation rates are more predictable and reproducible. Polyesters, such as polylactic acid (PLA) and poly(ε-caprolactone) (PCL), are the most commonly used synthetic polymer in bone tissue engineering. These polymers are biocompatible, non-cytotoxic and demonstrated to have suitable degradation rates [15,16]. Alternatively, α-amino acid based poly(ester amide) (PEA) and poly(ester urea) (PEU) belong to a class of synthetic polymers with promising properties in biomedical field. Indeed, these polymers can combine the biodegradability of polyesters and the mechanical and thermal behavior of polyamides [17,18]. The presence of the α-amino acids in the PEA and PEU's structure improves cell-material interactions and provides the polymers with the ability to be degraded by enzymes. Additionally, if α-amino acids with reactive pendant groups (–OH, $–NH_2$, –COOH, –SH) are used, the further post-functionalization of the polymers with moieties of interest is possible [19]. For instance, a PEU based on tyrosine was used to attach osteogenic growth peptide or bone morphogenetic protein-2 as a way to improve osteogenic differentiation [20,21]. PEAs and PEUs can be prepared with a myriad of structures, allowing to tailor their properties to a specific application [19].

Scaffolds for bone tissue engineering must be biocompatible and, thereby, cells must be able to adhere to their surfaces and proliferate. They should have an interconnected porous structure with pore sizes greater than 100 μm for enabling cell adhesion and proliferation, nutrient/waste transportation and bone ingrowth. The mechanical properties should ideally be similar to those of host bone, and the degradation rate should match the rate of new bone formation [22]. Marine skeletons, mainly composed by aragonite ($CaCO_3$), have been explored as an attractive source to obtain CaP scaffolds via a hydrothermal treatment (HT) [23]. Cuttlefish bone (CB), the hard tissue in cuttlefish, is a widely available and inexpensive material. It is composed by an internal lamellar matrix and a dorsal shield. The lamellar matrix has a quasi-periodic microstructure organized by lamellae supported by pillars, which form channels with an elevated degree of interconnectivity. This unique architecture has a porosity of approximately 93% and pore sizes varying between 200 and 600 μm [24]. In this regard, among the different marine skeletons, CB is one of the most studied materials for bone grafts. Rocha et al. [25,26] were the first ones to obtain CB-derived HA scaffolds via HT. The original structure was fully preserved in the HA scaffolds and the *in vitro* and *in vivo* studies demonstrated their osteoinductive properties, promoting excellent cell adhesion, proliferation and differentiation [25–27]. To improve the biological performance, fluorine ($F^-$) [28] and silicon ($Si^{4+}$) [29] were incorporated into the obtained scaffolds. On the other hand, and recognizing the brittleness of the HA scaffolds derived from CB, Milovac et al. [30,31] and Kim et al. [32] coated the scaffolds with PCL and observed the improvement of mechanical and biological behaviors. In order to have an effective improvement of the mechanical properties, Milovac et al. [31] coated the scaffolds with a 20 % (w/v) of PCL solution. But considering the slow degradation of PCL, Rogina et al. [33] coated HA scaffolds

derived from CB with a combination of PCL and PLA. Through the combination of these two polymers, it was possible to reduce the polymer thickness and improve the mechanical properties.

The present work aims at obtaining via HT CB-derived BCP scaffolds incorporating different doping ions ($Sr^{2+}$, $Mg^{2+}$ and $Zn^{2+}$) in various combinations. The surface of the scaffolds was further functionalized with PCL, poly(DL-lactide) (PDLA), PEA and PEU coatings by using vacuum impregnation. The chemical composition, morphological properties and mechanical properties were examined. The capacity of coated scaffolds to induce the precipitation of a calcium phosphate layer on its surface was investigated.

## 2. Materials and methods

### 2.1 Preparation of non-doped and doped BCP scaffolds derived from CB

Di-ammonium hydrogen phosphate [$(NH_4)_2HPO_4$, Panreac AppliChem, Spain] was used as precursor for phosphorous (P). Nitrate salts were adopted as precursors for the cationic ($Sr^{2+}$, $Mg^{2+}$, $Zn^{2+}$) dopants, namely, Strontium nitrate, $Sr(NO_3)_2$, Magnesium nitrate hexahydrate, $Mg(NO_3)_2$ $6H_2O$, and zinc nitrate hexahydrate, $Zn(NO_3)_2$ $6H_2O$, all from Sigma-Aldrich, Germany. CBs obtained from cuttlefish, *Sepia officinalis* were used as calcium source. In order to evaluate the exact amount of water, organic matter and $CaCO_3$, raw CB samples were subjected to differential and gravimetric thermal analyses (DTA/TG, Labsys Setaram TG-DTA/DSC, France), using a heating rate of 10 ºC $min^{-1}$. The exact content of $CaCO_3$ was determined and taken into account upon mixing with the required amounts of the other reagents. The lamella of raw CB was firstly cut into small pieces, washed with water, and dried before being

used as starting materials for the preparation of non-doped and doped BCP scaffolds derived from the CB. The CB pieces with a known amount of $CaCO_3$ were mixed with the required amount and concentration of the phosphorous (P) precursor solution to obtain the desired non-doped BCP composition. For the doped scaffolds, an additional solution containing the required propositions of the cationic nitrate precursor salts was also prepared and mixed with the phosphorous solution. Four different doped compositions with a fixed $Sr^{2+}$ content (6 mol%, BCP-6Sr), alone or in various combinations with other doping ions (2 mol% $Mg^{2+}$, BCP-6Sr2Mg; 2 mol% $Zn^{2+}$, BCP-6Sr2Zn; and 2 mol% $Mg^{2+}$ + 2 mol% $Zn^{2+}$, BCP-6Sr2Mg2Zn) were prepared.

The reacting solutions and the CB pieces were then sealed in poly(tetrafluorethylene) (PTFE) lined stainless steel autoclaves and placed at 200 ºC for 24 h in the oven. The obtained scaffolds were washed with distilled water and dried in an oven at 40 ºC. Afterwards, the scaffolds were heat treated at 700 ºC with a heating rate of 0.5 ºC·min$^{-1}$ for 1 h to eliminate the organic material and, then, sintered at 1200 ºC for 2 h, using a heating rate of 2 ºC min$^{-1}$.

**2.2 Polymeric coatings**

BCP scaffolds were coated with two of the most used polymers in the biomedical field, PCL (CAPA$^{TM}$6800 $M_n$ = 80.000 g mol$^{-1}$) or PDLA (PURASORB® PDL 20, $M_w$ = 47365 g mol$^{-1}$), purchased from Perstorp Specialty Chemicals AB (Perstorp, Sweden) and Corbion Purac (Amsterdam, The Netherlands), respectively. In addition, PEA or PEU, which were synthesized in the laboratory (see Supporting Information for the synthesis details and chemical characterization of the polymers, Fig. S1 and Fig. S2), were also used for the coating of BCP scaffolds. Both PCL and PDLA were dissolved in dichloromethane (Sigma-Aldrich, Germany) at concentrations of 5 %

and 3 % (w/v), respectively. On the other hand, PEA and PEU were dissolved in chloroform (Fisher Scientific, United Kingdom) at a concentration of 5 % (w/v). The addition of 1 ml of *N, N'*-dimethylformamide (Sigma-Aldrich, Germany) was required to improve the dissolution of these polymers.

The prepared scaffolds were dipped in the polymer solutions under partial vacuum for approximately 5 min. The vacuum allows the removal of air from the pores and ensures that the polymer solution can be easily impregnated into the porous structure. The coated samples were dried in an oven overnight and were, posteriorly, placed at room temperature (RT) for more 7 days to eliminate the remaining organic solvent.

### 2.3 Characterization

The crystalline phases of all the synthesized (non-doped and doped) CB-derived BCP scaffolds were identified by X-ray diffraction (XDR) using a High Resolution X-ray Diffractometer (PANalytical X'Pert PRO) with Cu Kα radiation (λ = 1.5406 Å) produced at 40 mA and 45 kV. Data were collected in the 2θ range between 10º and 100º with a 2θ-step size of 0.0260º per second. The Rietveld refinements were performed using the software TOPAS 5.0 (Bruker AXS, Karlsruhe, Germany) with the fundamental parameters. To identify the crystalline phases it was used the ICDD card numbers of # 04-015-7545 for HA and # 04-006-9376 for β-TCP.

Inductively couple plasma (ICP) spectrometry (ICP-OES Jobin Yvon Activa M., USA) was used for the elemental analysis of Sr, Mg and Zn. Before analyses, the powders were dissolved in 2% nitric acid ($HNO_3$).

The identification of the characteristic functional groups and structural characterization was obtained by Fourier transform infrared (FTIR) spectroscopy using

a FTIR Bruker Tensor 27 equipped with a Golden Gate Single Reflection Diamond ATR. The data are collected over the spectral range of 400–4000 $cm^{-1}$ using a total of 256 scans and a spectral resolution of 4 $cm^{-1}$, having the sample placed directly over the diamond crystal and pressed.

The $^{1}H$ NMR spectra of the PEA and PEU was obtained at 25 ºC on a Bruker Avance 400 MHz Spectrometer (Billerica, Massachusetts, EUA) using a 5 mm broadband NMR probe, in DMSO-*d*6. Tetramethylsilane was used as the internal standard.

The interconnectivity of the CB microstructure was assessed by micro computed tomography (µ-CT, Bruker) using an exposure time of 800 ms, energy of 50 kV and intensity of 200 µA. The NRecon software was used for the reconstruction of cross-section images. The microstructure and morphology of the raw CB scaffolds, and after hydrothermal transformation, without and with the polymeric coatings were observed by scanning electron microscopy (SEM, Hitachi SU-70, Hitachi High-Technologies Europe, GmbH, Germany).

Density measurements using the buoyancy (Archimedes') method was employed to analyze whether the porosity changes after transformation and how it was affected by the polymeric coating. Thus, raw CB and the hydrothermally transformed and sintered scaffolds, without and with the polymeric coatings were immersed in distilled water in accordance with the European Standard EN 993-1. The scaffolds density was calculated using the following equation:

$$\rho_{scaffold} = \frac{m_1}{m_3 - m_2} \times \rho_w$$

where $\rho_{scaffold}$ and $\rho_w$ are respectively the densities of the scaffold and of water in g $cm^{-3}$; $m_1$ is the weight of the dried scaffold (g), $m_2$ is the weight of the scaffold suspended in water (g), and $m_3$ is the weigth of the water saturated scaffold measured in

air (g). By knowing the mineralogical phase compositions and, if applicable, the percentage of adsorbed polymer in each sample, it is possible to calculate the theorethical density of the scaffold and, then, its porosity.

The compression tests were carried out in using a universal testing machine (AG-IS10kN, Shimadzu, Kyoto, Japan) by applying perpendicularly to the lamella a maximum load of 200 N to cubic shape scaffolds with approximately 3 mm side at a constant crosshead speed of 0.5 mm $min^{-1}$ under dry ambient conditions.

### 2.4 *In vitro* bio-mineralization

The *in vitro* bio-mineralization capacity of the scaffolds was analyzed by immersion of the uncoated and coated scaffolds in simulated body fluid (SBF) at 37 ºC in an orbital shaker for 3, 7 and 14 days. The SBF solution was prepared accordingly to the international standard ISO 23317. The *in vitro* bio-mineralization tests were performed according to an unified procedure described elsewhere [34] using a standard area per mL of SBF solution of 0.5 $cm^2$ $mL^{-1}$. After each soaking period, the samples were removed from SBF solution, gently rinsed with distilled water and then left to dry in a desiccator. Once dried, the scaffolds were analyzed by SEM to observe the bioactive layer deposited onto their surfaces.

### 2.5 Statistical analysis

The experiments were performed in triplicated and the values are expressed as mean ± standard deviation. The statistical analysis was performed using one-way analysis of variance (ANOVA). $P < 0.05$ was considered statistically significant.

# 3. Results

## 3.1 Thermal analysis

The results of the thermal analysis (DTA and TG) of raw CB are shown in Fig. 1. The TG curve revealed a weight loss of 1.02% up to 150 ºC associated with water evaporation. The weight loss between 150 ºC and 500 ºC due to the burning of the organic matter was about 4.49%, and is associated with two exothermic peaks (DTA curve) at 285 and 430 ºC. Lastly, the weight loss of 38.64% over 500–1000 ºC was due to the decomposition of aragonite into calcium oxide. This thermal transformation is also responsible for the strong endothermic peak centered at 844 ºC.

## 3.2 Chemical and structural characterization

The XRD patterns of the HT scaffolds sintered at 1200 ºC are displayed in Fig. 2. The crystalline phases identified indicated the presence of HA (# 04-015-7245) and β-TCP (# 04-006-9376). Although all the synthesized compositions exhibited the same phases (HA and β-TCP), their propositions were dependent on the doping combinations. When $Sr^{2+}$ is incorporated alone in the crystalline lattice all the peaks are shifted to lower angles. On the other hand, when $Sr^{2+}$ is incorporated along with $Mg^{2+}$ or $Zn^{2+}$ in the crystalline lattice, there is an intensity enhancement and a shift to higher angles of the peaks corresponding to the β-TCP phase, while the HA peaks are shifted in the opposite direction. The concomitant incorporation of $Sr^{2+}$, $Mg^{2+}$ and $Zn^{2+}$ in the crystalline structure results in a slight overall shift of all the peaks to higher angles. The quantitative phase analysis data determined by Rietveld refinement (wt.%) for all compositions are summarized in Table 1.

The contents of the doping elements (Sr, Mg and Zn) in the BCP scaffolds were determined by ICP analysis. The experimentally measured values reported in Table 2 reveal that they are significantly below to the planned ones.

The FTIR spectra of the uncoated and coated (with different polymers) BCP scaffolds are shown in Fig. 3. All the uncoated scaffolds exhibit similar spectra with the characteristic vibrational modes of $-PO_4$ and –OH groups. The band at 475 $cm^{-1}$ is associated to doubly degenerate $\nu_2$ O–P–O bending. The bands at 550 and 600 $cm^{-1}$ correspond to the $PO_4$ tetrahedra $\nu_4$ mode and 1020 and 1087 $cm^{-1}$ represent the peaks for the $\nu_3$ mode. The bands at 940 and 960 $cm^{-1}$ denote the $\nu_1$ non-degenerate P–O symmetry stretching mode. The typical stretching and vibrational modes of –OH group should appear at 630 and 3575 $cm^{-1}$ [35]. Nevertheless, the band at 630 $cm^{-1}$ appears with a low intensity while the peak at 3575 $cm^{-1}$ did not appear at all. Overall, the FTIR spectra of the polymeric coated scaffolds appear as superpositions of individual BCP and polymer (PCL, PDLA, PEA or PEU) spectra. In FTIR spectra of the PCL coated samples the band at 1720 $cm^{-1}$ is due to the stretching vibrations of the C=O group in the ester linkage. The bands at 1460, 1390 and 1367 $cm^{-1}$ correspond to the $CH_2$ bending modes, and the 2942 and 2895 $cm^{-1}$ ones are ascribed to the $CH_2$ to the stretching mode. In addition, the bands at 1234, 1107 and 1042 $cm^{-1}$ correspond to the stretching vibrations of the C–O–C group of the ester linkage. The bands located at 1290 and 1160 $cm^{-1}$ are associated with the stretching of the C–C and C–O bonds of the ester group in the crystalline and amorphous phase, respectively [36]. The FTIR spectra of the PDLA coated samples exhibit the characteristic PDLA bands, although of low intensity. This can be understood considering that the coating was deposited from a relatively low concentrated [3 % (w/v)] PDLA solution, which results in a lower

percentage of polymeric coating. At 1745 $cm^{-1}$ is observed the stretching vibration of the C=O groups of the ester linkage. The peaks at 2998 and 2940 $cm^{-1}$ correspond to the stretching vibrations of the $C–CH_3$ and CH groups, respectively. The band at 1180 $cm^{-1}$ is ascribed to the stretching vibration of the C–O–C group and the $CH_3$ asymmetric deformation and symmetric wagging is observed at 1448 and 1375 $cm^{-1}$, respectively. The band located at 1043 $cm^{-1}$ is associated with stretching of the C–O bond and CH bending [37]. The FTIR spectra of PEA coated scaffolds show characteristic PEA peaks with the ester and amide linkages. The peak at 3300 $cm^{-1}$ corresponds to the stretching vibration of the N–H group of the amide linkage. The bands at 2890 and 2930 $cm^{-1}$ correspond to the symmetric and asymmetric stretching vibrations, respectively, of the $CH_2$ groups. The stretching vibration of the C=O group of the ester linkage appears at 1740 $cm^{-1}$. At 1650 and 1540 $cm^{-1}$ is possible to identify the bands ascribed to the amide I and II groups, respectively [38–40]. Lastly, the characteristic bands of PEU with the ester and urea linkages are observed in the PEU coated scaffolds. The band at 3390 $cm^{-1}$ corresponds to the stretching vibration of the N–H groups of the urea linkage. At 1565 $cm^{-1}$ is identified the band corresponding to both the bending of the N–H group and of the stretching of the C–N group of the urea linkage. The vibration of the C=O group of the ester and urea are identified at 1740 and 1625 $cm^{-1}$, respectively.

### 3.3 Microstructure

The unique CB architecture was observed by µ-CT and SEM (Fig. 4). The structure comprised by lamellae is supported by numerous pillars generating chambers with a height of approximately 400 µm. These chambers are separated by walls with a thickness of approximately 10 µm. Furthermore, the pillars create an interconnected porosity with widths between 100 and 260 µm that progress through the material in a

sigmoidal path. Moreover, it is evident the coating of the lamellar matrix with organic material, β-chitin. This interconnected porous structure was retained in all the compositions after HT and sintering (Fig. 5). Under a higher magnification, it is possible to observe the formation of CaP crystals and the morphological characteristics did not modify in the presence of the doping elements.

The morphology of the scaffolds from all BCP compositions after coating with the different polymers was also observed by SEM (Fig. 6). It is possible to observe that the surfaces of the scaffolds have been effectively covered with polymer layers, with most of the pores remaining unclogged. Moreover, it is possible to infer that the various polymers tested have different interactions with the inorganic matrix (Fig. 7a). These interactions could be a consequence of the viscosity of the polymeric solutions used for the coating (Fig. 7b). It was registered lower and similar viscosities for the 5 % (w/v) PEA and PEU solutions. Higher and also similar viscosity curves were obtained for the 5 % (w/v) PCL and 3 % (w/v) PDLA solutions. The highest viscosity curve was achieved with the 5 % (w/v) PDLA solution.

### 3.4 Porosity and mechanical properties

The porosity data reported in Table 3 reveal that the hydrothermal transformation and sintering processes did not affect the porous fraction of the scaffolds, as expected. The avegare percentages of porosity measured all the scaffolds are within the range of 92–93 %, being very similar to that of raw CB (92.85 ± 0.36 %). The polymeric coatings induced slight decreases in porosity, with the higher and similar porosities being registered for the scaffolds coated with PDLA, PEA or PEU. Porosity values slightly below 90 % were measured for the scaffolds coated with PCL.

The values of compressive strength (CS) and Young's modulus (YM) calculated from the maximum mechanical stress reached during the deformation period

are summarized in Table 4. The CS of the raw CB (1.63 ± 0.07 MPa) was drastically reduced by about 8 times after HT and sintering for BCP, BCP-6Sr and BCP-6Sr2Zn, and by about 4 times for the other compositions (BCP-6Sr2Mg, BCP-6Sr2Mg2Zn). Despite the differences in CS between the raw and the hydrothermaly transformed CB, both types of scaffolds exhibit similar stress-strain behaviors with the microstructure collapsing layer-by-layer (Fig. 8), instead of a catastrophic failure. The polymeric coatings significantly improved the CS, partially recovering the initial composite nature of the porous structures. The stress-strain plots displyed in Fig. 9 show that scaffolds undergo deformation but without the occurrence of a total collapse of the CB layers. In general, the higher values of CS and YM were achieved for the scaffolds coated with PEU. On the other hand, the lowest values were registered for the scaffolds coated with PEA. For instance, BCP-6Sr2Zn scaffolds improved the CS by almost 5 times from 0.20 ± 0.01 MPa to 0.97 ± 0.06 MPa after the coating with PEU.

### 3.5 *In vitro* bio-mineralization

The *in vitro* bio-mineralization occurred after immersion the scaffolds into SBF solution was analysed by SEM (Fig. 10.) After 14 days of incubation, all the scaffolds compositions exhibited the deposition of isolated or aggregated calcium phosphate microspheres, characteristic from the apatite developed *in vitro*. Despite knowing that the mineralization process is affected by the nature of the polymer, it was observed similar mineralizations for the different polymeric coating with exception of the scaffolds coated with PEA. The EDS analysis of the obtained particles showed presence of Ca, P and O and small quantities of Na, Mg and Cl, characteristic of the natural apatite of the human bone.

## 4. Discussion

In this study, we obtained undoped and ion ($Sr^{2+}$, $Mg^{2+}$ and $Zn^{2+}$) doped BCP scaffolds derived from CB. Different polymers (PCL, PDLA, PEA and PEU) were used for the polymeric coating in order to achieve better mechanical properties.

Rocha et al. [26] were the first authors to report the transformation of CB into HA scaffolds by HT. Since then, the reseach works have been mainly focoused on the transformation of CB into HA scaffolds. Nevertheless, it is recognize that BCP (HA + β-TCP) biomaterials enable to obtain a better balance between resorption and solubilization and, consequently, ensuring the stability of the material while promoting bone ingrowth. In this vein, Sarin et al. [41] attempted to produced BCP scaffolds derived from CB by immersion the raw CB into a phosphoric acid solution, but only a partial conversion extent was achieved, as the final product presented a significant amount of CaO (~6.4 wt.%). This is not desired as the remaining CaO will react with the physiological fluid after implantation forming calcium hydroxide and creating a cytotoxic high pH environment [42,43]. In the present work, a complete transformation of CB into a BCP scaffold was achieved for both undoped and doped scaffolds. Accordingly, beyond HA and β-TCP, no other crystalline phases were observed by XRD (Fig. 2) and the Rietveld refinement (Table 1). The obtained FTIR spectra of the samples revealed the presence of the $–PO_4$ groups and a very small content of –OH groups, which might be a consequence of the absence of –OH group in the β-TCP phase, or the occurrence of a partial de-hydroxylation of HA at 1200 ºC. But the very low content of –OH groups in biological apatites is also well recognized [44]. Regarding the volatile nature of carbonates and the sintering temperature of the scaffolds (1200 ºC), the carbonate peaks in apatites (872, 1412, 1458 and 1547 $cm^{-1}$)

did not appear in the FTIR spectra of all the samples [26]. The FTIR data are therefore in good agreement with the XRD results (Fig. 2).

The incorporation of doping elements into the crystalline lattices of CaP has been adopted as a strategy to improve the biological performance of CB-derived scaffolds. Kannan et al. [28] and Kim et al. [29] studied the incorporation of $F^-$ and $Si^{4+}$, respectively. This work was more ambitious aiming at the concomitant incorporation of some essential ions ($Sr^{2+}$, $Mg^{2+}$ and $Zn^{2+}$) into the BCP structure. Although the diffraction patterns of all the samples are more or less coincident with HA and β-TCP, the effects of doping with ions having different radii are reflected in the shifts observed in the XRD peaks. For instance, the incorporation of $Sr^{2+}$ into the crystal lattice (BCP-6Sr) resulted in a slight shift to lower angles. This is consistent with an increase in the lattice parameters, as expected from the partial replacement of $Ca^{2+}$ (0.99 Å) by the larger size ion ($Sr^{2+}$ 1.20 Å) in the lattice sites of HA and β-TCP [45]. This is a clear indication that $Sr^{2+}$ has been effectively incorporated in both crystalline phases [45–50]. The incorporation of $Sr^{2+}$ together with $Mg^{2+}$ (BCP-6Sr2Mg) or with $Zn^{2+}$ (BCP-6Sr2Zn) resulted in shifts of the HA and β-TCP peaks to lower and higher angles, respectively. The slight shift of the β-TCP peaks to higher angles means that the smaller $Mg^{2+}$ (0.69 Å) and $Zn^{2+}$ (0.74 Å) ions were preferentially incorporated in the β-TCP phase. This is not much surprising considering these smaller ions tend to enhance the stability of β-TCP, which has been extensively reported, particularly for $Mg^{2+}$ [48,49,51,52]. Moreover, in the presence of $Mg^{2+}$ or $Zn^{2+}$ there is an intensity enhancement of the β-TCP peaks. This confirms the preference of these doping ions for occupying lattice positions in the β-TCP phase, enhancing its stability. Under these circumstances, the $Sr^{2+}$ ions that can almost equally be accommodated in any of the crystalline lattices (HA or β-TCP) will compete with the $Ca^{2+}$ ions replaced in the β-

TCP phase for available positions in the crystalline lattice of HA. The resulting increase in the lattice parameters of HA explains the observed shift of the XRD peaks to lower angles. On the other hand, the incorporation of $Sr^{2+}$ together with $Mg^{2+}$ and $Zn^{2+}$ (BCP-6Sr2Mg2Zn) resulted in an apparent slight shift of all the peaks to higher angles, what is somehow surprising. Despite the shifts of the XRD peaks, the elementary analysis shown in Table 2 demonstrates that doping elements encounter some difficulties in entering the lattice structure to replace calcium, attributed to ionic size mismatches.

An interconnected porous structure is a crucial parameter for cell proliferation, vascularization and nutrient supply. Thereby, such interconnected porous structure is beneficial for bone growth [22]. Recognizing the optimal pore size and interconnectivity of the CB, a significant number of research works [25–32,41,53,54] demonstrated that the initial CB structure could be preserved. Following the same principle, in this work it was observed by SEM (Fig. 4 and Fig. 5) that the HT and the ionic substitutions did not jeopardize the internal structure of CB. Moreover, the increasing surface roughness after the HT and sintering is beneficial for bone growth because it influences not only the cell adhesion and migration but also the production of extracellular matrix [55].

Raw CB is a composite with an inorganic phase ($CaCO_3$) and an organic phase (β-chitin) that covers the inorganic matrix [24]. However, the organic part is removed upon HT and sintering. The elimination of the organic component is intrinsically related to the decrease in the mechanical properties observed for all the different scaffold compositions (Fig. 7 and Table 4). In raw CB, the β-chitin is responsible for the redistribution of the compressive stress and dissipate the mechanical energy during deformation, increasing the resilience and toughness of the composite material, thereby, hindering the propagation of cracks [31]. Thus, β-chitin plays an important role in

conferring to the CB the functional and highly sophisticated features that enable cuttlefish maintaining its neutral buoyancy at a high depths, while retaining enough stiffness and strength to prevent sever distortion or crushing under the high hydrostatic pressures in deep water [56–58]. The elimination of the organic matter during the HT and sintering processes severely degrades the mechanical properties of CB.

To overcome this drawback and improving the mechanical properties of CB-derived HA scaffolds, Milovac et al. [31] and Kim et al. [32] impregnated them with PCL solutions, which were then evaporated to leave coatings deposited in the porous cell walls. A coating of the CB-derived HA scaffolds with a combination of PCL and PLA was studied by Rogina et al. [33].

The polymeric coatings applied to CB-derived BCP scaffolds aimed at improving their mechanical properties. Besides PCL or PDLA (two of the most widely used polymers in the biomedical field), coatings based on PEA or PEU (polymers with an increasing relevance for biomedical applications [19]) were also investigated in the present work. The presence of the polymers in the coated scaffolds was confirmed by FTIR through their characteristic peaks appearing superposed with those of BCP peaks. Importantly, the polymeric coatings had no significant negative impact on the porosity (Table 3), except in the case of the most viscous 5 % (w/v) PDLA solution. Accordingly, a more diluted solution [3 % (w/v)] was adopted for further coatings with this polymer. Under this condition, the porosity values of PDLA coated scaffolds were similar to the PEA and PEU coated scaffolds. The lowest value of porosity (~89%) registered for scaffolds coated with PCL from a 5 % (w/v) solution, which can also be attributed to its relatively high viscosity, limiting the solution runoff from the pores.. The 5 % (w/v) PEA and PEU solutions exhibited the lower viscosities, being able to penetrate into the intrinsic porosity of cell walls and easily runoff, forming thinner

coating layers in comparison to PCL and PDLA. For instance, a reduction in the concentration of the PCL solution to 1 % (w/v) (Fig. S4) was required to achieve viscosity curves similar to the ones corresponding to the 5 % (w/v) PEA and PEU solutions. The specific interactions between the functional groups of the different polymers and the CaP substrates are also likely to play an important role in determining the features of the coatings. The –COOH groups present in all polymers exhibit a high affinity for calcium. In addition to –COOH group, the PEA and PEU polymers exhibit $–NH_2$ as terminal groups, which have chemical affinity towards phosphorous [59]. These affinities could justify also the enhanced interactions of the PEA and PEU with the CaP scaffolds.

Regarding the mechanical properties, the coating significantly improved the CS. The vaccum impregnation allowed the an efficient filling of the defects, thus mitigating the crack propagation in the scaffolds. In this vein, instead of a layer-by-layer collapse, it was observed a deformation of the scaffolds with small and less pronounced cracks. Regarding the PCL coated scaffolds, the results are in agreement with those of Kim et al.[32]. The authors obtained an improvement of the mechanical properties by 2.09-fold upon the coating with 5 % PCL. In our study, the mechanical properties of the BCP scaffolds coated with 5 % PCL improved 2.95-fold. Although the CS values registered for the scaffolds coated with PEA are generally lower , the stress-deformation curves are more stable. This feature can be attributed to a better interaction between the PEA and the inorganic matrix (Figure 8). The higher values of mechanical strength were registered with PEU coating. For instance, an improvement by 4.70-fold was obtained for the BCP-6Sr2Zn scaffolds. Typically, the values of CS and YM of human trabecular bone vary between 0.1–16 MPa and between 50–500 MPa, respectively [60]. Thus, the CS and YM registered for our composite scaffolds are respectively above, and below,

the lower limits of the ranges reported for trabecular bone. These relatively low values are understandable considering the intrinsically high porosity of the scaffolds. Further enhancements of mechanical properties are likely achievable by repeating the dipping process, while taking care for do not excessively compromising the porosity.

The material capacity to bond the natural bone upon implantation is normally evaluated by immersion in SBF solution, which is recognized as a powerful technique to predicting the bioactivity of a material [61]. The apatite formation on the polymeric coated scaffolds is dependent on the functional group on the polymer surface. Negatively charged groups, like $–COO^-$, strongly induced apatite formation as they bind to $Ca^{2+}$, which promote the apatite nucleation and growth. On the other hand, the apatite formation in the presence of positive groups, like $–NH_3^+$, is significantly lower [62]. The four used polymers originate –COOH groups during hydrolysis. However, for PEA the pH drop is very small because $–NH_2$ groups are also formed, being a well-known advantage of these polymers. As consequence, a lower concentration of –COOH is available for complexation with $Ca^{2+}$ and less amount of apatite is formed.

## 5. Conclusions

Raw CB was, for the first time, completely hydrothermally converted into undoped and ion ($Sr^{2+}$, $Mg^{2+}$ and/or $Zn^{2+}$) doped BCP scaffolds while maintaining their internal structure. This transformation and the subsequent heat treatment removed the organic (β-chitin) phase matrix existing in the raw CB, negatively affecting the mechanical properties of the scaffolds. To overcome this problem, different polymers (PCL, PDLA, PEA or PEU) were used to coat the scaffolds. The polymers did enhance the mechanical properties of the scaffolds. However, PEU was generally more effective in upgrading the compressive strength to values registered for human trabecular bone

(0.93 – 1.73 MPa). Moreover, after the polymeric coating the scaffolds exhibited a good *in vitro* bioactivity in SBF. These scaffolds are worthy of further investigation as potential candidates for bone tissue engineering applications.

## Acknowledgements

This work was developed within the scope of the project CICECO-Aveiro Institute of Materials, FCT Ref. UID/CTM/50011/2019, financed by national funds through the FCT/MCTES. Ana S. Neto acknowledges to AdvaMTech, the PhD Program on Advanced Materials and Processing for the PhD grant, PD/BD/114132/2015, founded by the Portuguese Foundation for Science and Technology (FCT). The authors are very thankful to Dias de Sousa - Instrumentação Analítica e Científica, S.A., Setúbal, Portugal, for doing the µ-CT analysis of our samples.

## References

[1] M.K. Sen, T. Miclau, Autologous iliac crest bone graft: should it still be the gold standard for treating nonunions?, Injury. 38 Suppl 1 (2007) S75–S80. doi:10.1016/j.injury.2007.02.012.

[2] L. Roseti, V. Parisi, M. Petretta, C. Cavallo, G. Desando, I. Bartolotti, B. Grigolo, Scaffolds for Bone Tissue Engineering: State of the art and new perspectives, Mater. Sci. Eng. C. 78 (2017) 1246–1262. doi:10.1016/j.msec.2017.05.017.

[3] S. V. Dorozhkin, Calcium Orthophosphates as Bioceramics: State of the Art, J. Funct. Biomater. 1 (2010) 22–107. doi:10.3390/jfb1010022.

[4] R.Z. Legeros, Calcium Phosphate Materials in Restorative Dentistry: a Review, Adv. Dent. Res. 2 (1988) 164–180. doi:10.1177/08959374880020011101.

[5] J.M. Bouler, P. Pilet, O. Gauthier, E. Verron, Biphasic calcium phosphate ceramics for bone reconstruction: A review of biological response, Acta Biomater. 53 (2017) 1–12. doi:10.1016/j.actbio.2017.01.076.

[6] C. Castellani, G. Zanoni, S. Tangl, M. Van Griensven, H. Redl, Biphasic calcium phosphate ceramics in small bone defects: Potential influence of carrier substances and bone marrow on bone regeneration, Clin. Oral Implants Res. 20 (2009) 1367–1374. doi:10.1111/j.1600-0501.2009.01760.x.

[7] S.E. Lobo, T.L. Arinzeh, Biphasic calcium phosphate ceramics for bone regeneration and tissue engineering applications, Materials (Basel). 3 (2010) 815–826. doi:10.3390/ma3020815.

[8] E. Boanini, M. Gazzano, A. Bigi, Ionic substitutions in calcium phosphates synthesized at low temperature, Acta Biomater. 6 (2010) 1882–1894. doi:10.1016/j.actbio.2009.12.041.

[9] E.A. Botchwey, S.R. Pollack, E.M. Levine, C.T. Laurencin, Bone tissue engineering in a rotating bioreactor, J. Biomed. Mater. Res. - Part A. 55 (2001) 242–253. doi:10.1016/j.micinf.2011.07.011.Innate.

[10] E. O'Neill, G. Awale, L. Daneshmandi, O. Umerah, K.W.H. Lo, The roles of ions on bone regeneration, Drug Discov. Today. 23 (2018) 879–890. doi:10.1016/j.drudis.2018.01.049.

[11] A.S. Prasad, Zinc is an Antioxidant and Anti-Inflammatory Agent: Its Role in Human Health, Front. Nutr. 1 (2014) 1–10. doi:10.3389/fnut.2014.00014.

[12] A.R. Shrivats, M.C. McDermott, J.O. Hollinger, Bone tissue engineering: state of the union.,

Drug Discov. Today. 19 (2014) 781–786. doi:10.1016/j.drudis.2014.04.010.
[13] R.Y. Basha, S.K. T.S., M. Doble, Design of biocomposite materials for bone tissue regeneration, Mater. Sci. Eng. C. 57 (2015) 452–463. doi:10.1016/j.msec.2015.07.016.
[14] K.E. Tanner, Bioactive composites for bone tissue engineering, Procedings Inst. Mech. Eng. H. 224 (2010) 1359–1372. doi:10.1243/09544119JEIM823.
[15] M.I. Sabir, X. Xu, L. Li, A review on biodegradable polymeric materials for bone tissue engineering applications, J. Mater. Sci. 44 (2009) 5713–5724. doi:10.1007/s10853-009-3770-7.
[16] M.S. Cortizo, M.S. Belluzo, Biodegradable Polymers for Bone Tissue Engineering, in: S.N. Goyanes, N.B. D'Accorso (Eds.), Ind. Appl. Renew. Biomass Prod. Past, Present Futur., 2017. doi:10.1007/978-3-319-61288-1.
[17] A. Rodriguez-Galan, L. Franco, J. Puiggali, Degradable poly(ester amide)s for biomedical applications, Polymers (Basel). 3 (2011) 65–99. doi:10.3390/polym3010065.
[18] A.C. Fonseca, J.F.J. Coelho, M.H. Gil, P.N. Simões, Poly(ester amide)s based on l-lactic acid oligomers and glycine: the role of the central unit of the l-lactic acid oligomers and their molecular weight in the poly(ester amide)s properties, Polym. Bull. 71 (2014) 3085–3109. doi:10.1007/s00289-014-1239-6.
[19] A.C. Fonseca, M.H. Gil, P.N. Simões, Biodegradable poly(ester amide)s - A remarkable opportunity for the biomedical area: Review on the synthesis, characterization and applications, Prog. Polym. Sci. 39 (2014) 1291–1311. doi:10.1016/j.progpolymsci.2013.11.007.
[20] K.S. Stakleff, F. Lin, L.A. Smith Callahan, M.B. Wade, A. Esterle, J. Miller, M. Graham, M.L. Becker, Resorbable, amino acid-based poly(ester urea)s crosslinked with osteogenic growth peptide with enhanced mechanical properties and bioactivity, Acta Biomater. 9 (2013) 5132–5142. doi:10.1016/j.actbio.2012.08.035.
[21] S. Li, Y. Xu, J. Yu, M.L. Becker, Enhanced osteogenic activity of poly(ester urea) scaffolds using facile post-3D printing peptide functionalization strategies, Biomaterials. 141 (2017) 176–187. doi:10.1016/j.biomaterials.2017.06.038.
[22] F.J. O'Brien, Biomaterials & scaffolds for tissue engineering, Mater. Today. 14 (2011) 88–95. doi:10.1016/S1369-7021(11)70058-X.
[23] X. Zhang, K.S. Vecchio, Conversion of natural marine skeletons as scaffolds for bone tissue engineering, Front. Mater. Sci. 7 (2013) 103–117. doi:10.1007/s11706-013-0204-x.
[24] J.D. Birchall, N.L. Thomas, On the architecture and function of cuttlefish bone, J. Mater. Sci. 18 (1983) 2081–2086. doi:10.1007/BF00555001.
[25] J.H.G. Rocha, A.F. Lemos, S. Agathopoulos, S. Kannan, P. Valério, J.M.F. Ferreira, Hydrothermal growth of hydroxyapatite scaffolds from aragonitic cuttlefish bones, J. Biomed. Mater. Res. - Part A. 77 (2006) 160–168. doi:10.1002/jbm.a.30566.
[26] J.H.G. Rocha, A.F. Lemos, S. Agathopoulos, P. Valério, S. Kannan, F.N. Oktar, J.M.F. Ferreira, Scaffolds for bone restoration from cuttlefish, Bone. 37 (2005) 850–857. doi:10.1016/j.bone.2005.06.018.
[27] L. Hongmin, Z. Wei, Y. Xingrong, W. Jing, G. Wenxin, C. Jihong, X. Xin, C. Fulin, Osteoinductive nanohydroxyapatite bone substitute prepared via in situ hydrothermal transformation of cuttlefish bone, J. Biomed. Mater. Res. - Part B Appl. Biomater. 103B (2015) 816–824. doi:10.1002/jbm.b.33261.
[28] S. Kannan, J.H.G. Rocha, S. Agathopoulos, J.M.F. Ferreira, Fluorine-substituted hydroxyapatite scaffolds hydrothermally grown from aragonitic cuttlefish bones, Acta Biomater. 3 (2007) 243–249. doi:10.1016/j.actbio.2006.09.006.
[29] B.S. Kim, S.S. Yang, J.H. Yoon, J. Lee, Enhanced bone regeneration by silicon-substituted hydroxyapatite derived from cuttlefish bone, Clin. Oral Implants Res. 00 (2015) 1–8. doi:10.1111/clr.12613.
[30] D. Milovac, T.C. Gamboa-Martínez, M. Ivankovic, G. Gallego Ferrer, H. Ivankovic, PCL-coated hydroxyapatite scaffold derived from cuttlefish bone: In vitro cell culture studies, Mater. Sci. Eng. C. 42 (2014) 264–272. doi:10.1016/j.msec.2014.05.034.
[31] D. Milovac, G. Gallego Ferrer, M. Ivankovic, H. Ivankovic, PCL-coated hydroxyapatite scaffold derived from cuttlefish bone: Morphology, mechanical properties and bioactivity, Mater. Sci. Eng. C. 34 (2014) 437–445. doi:10.1016/j.msec.2014.05.034.
[32] B.S. Kim, H.J. Kang, J. Lee, Improvement of the compressive strength of a cuttlefish bone-derived porous hydroxyapatite scaffold via polycaprolactone coating, J. Biomed. Mater. Res. - Part B. 101 (2013) 1302–1309. doi:10.1002/jbm.b.32943.
[33] A. Rogina, M. Antunovic, D. Milovac, Biomimetic design of bone substitutes based on cuttlefish bone-derived hydroxyapatite and biodegradable polymers, J. Biomed. Mater. Res. - Part B. 107B (2018) 197–204.

[34] A.C. Popa, G.E. Stan, M.A. Husanu, I. Mercioniu, L.F. Santos, H.R. Fernandes, J.M.F. Ferreira, Bioglass implant-coating interactions in synthetic physiological fluids with varying degrees of biomimicry, Int. J. Nanomedicine. 12 (2017) 683–707. doi:10.2147/IJN.S123236.

[35] S. Raynaud, E. Champion, D. Bernache-Assollant, P. Thomas, Calcium phosphate apatites with variable Ca/P atomic ratio I. Synthesis, characterisation and thermal stability of powders, Biomaterials. 23 (2002) 1065–1072. doi:10.1016/S0142-9612(01)00218-6.

[36] A. Elzubair, C.N. Elias, J.C.M. Suarez, H.P. Lopes, M.V.B. Vieira, The physical characterization of a thermoplastic polymer for endodontic obturation, J. Dent. 34 (2006) 784–789. doi:10.1016/j.jdent.2006.03.002.

[37] D. Mao, Q. Li, D. Li, Y. Chen, X. Chen, X. Xu, Fabrication of 3D porous poly(lactic acid)-based composite scaffolds with tunable biodegradation for bone tissue engineering, Mater. Des. 142 (2018) 1–10. doi:10.1016/j.matdes.2018.01.016.

[38] X. Pang, C.C. Chu, Synthesis, characterization and biodegradation of functionalized amino acid-based poly(ester amide)s, Biomaterials. 31 (2010) 3745–3754. doi:10.1016/j.biomaterials.2010.01.027.

[39] D.J. Skrovanek, S.E. Howe, P.C. Painter, M.M. Coleman, Hydrogen Bonding in Polymers: Infrared Temperature Studies of an Amorphous Polyamide, Macromolecules. 18 (1985) 1676–1683.

[40] B. Kaczmarczyk, S. e. ˛, Danuta, Hydrogen bonds in poly(ester amide)s and their model compounds, Polymer (Guildf). 36 (1995) 5019–5025. doi:10.1016/0032-3861(96)81631-4.

[41] P. Sarin, S.J. Lee, Z.D. Apostolov, W.M. Kriven, Porous biphasic calcium phosphate scaffolds from cuttlefish bone, J. Am. Ceram. Soc. 94 (2011) 2362–2370. doi:10.1111/j.1551-2916.2011.04404.x.

[42] F.A. Guiotti, M.C. Kuga, M.A.H. Duarte, A. Sant'Anna Júnior, G. Faria, Effect of calcium hydroxide dressing on push-out bond strength of endodontic sealers to root canal dentin, Braz. Oral Res. 28 (2014) 1–6. doi:10.1590/S1806-83242014.50000002.

[43] A.R. Butt, S. Ejaz, J.C. Baron, M. Ikram, S. Ali, S. Applications, CaO nanoparticles as a potential drug delivery agent for biomedical applications, Diget J. Nomaterials Biostructures. 10 (2015) 799–809.

[44] J.D. Pasteris, B. Wopenka, J.J. Freeman, K. Rogers, E. Valsami-Jones, J.A.M. Van Der Houwen, M.J. Silva, Lack of OH in nanocrystalline apatite as a function of degree of atomic order: implications for bone and biomaterials, Biomaterials. 25 (2004) 229–238. doi:10.1016/S0142-9612(03)00487-3.

[45] A. Bigi, E. Boanini, C. Capuccini, M. Gazzano, Strontium-substituted hydroxyapatite nanocrystals, Inorganica Chim. Acta. 360 (2007) 1009–1016. doi:10.1016/j.ica.2006.07.074.

[46] C. Capuccini, P. Torricelli, E. Boanini, M. Gazzano, R. Giardino, A. Bigi, Interaction of Sr-doped hydroxyapatite nanocrystals with osteoclast and osteoblast-like cells, J. Biomed. Mater. Res. - Part A. 89 (2009) 594–600. doi:10.1002/jbm.a.31975.

[47] U. Thormann, S. Ray, U. Sommer, T. ElKhassawna, T. Rehling, M. Hundgeburth, A. Henß, M. Rohnke, J. Janek, K.S. Lips, C. Heiss, G. Schlewitz, G. Szalay, M. Schumacher, M. Gelinsky, R. Schnettler, V. Alt, Bone formation induced by strontium modified calcium phosphate cement in critical-size metaphyseal fracture defects in ovariectomized rats, Biomaterials. 34 (2013) 8589–8598. doi:10.1016/j.biomaterials.2013.07.036.

[48] C.F. Marques, A. Lemos, S.I. Vieira, O.A.B. Da Cruz E Silva, A. Bettencourt, J.M.F. Ferreira, Antibiotic-loaded Sr-doped porous calcium phosphate granules as multifunctional bone grafts, Ceram. Int. 42 (2016) 2706–2716. doi:10.1016/j.ceramint.2015.11.001.

[49] C.F. Marques, S. Olhero, J.C.C. Abrantes, A. Marote, S. Ferreira, S.I. Vieira, J.M.F. Ferreira, Biocompatibility and antimicrobial activity of biphasic calcium phosphate powders doped with metal ions for regenerative medicine, Ceram. Int. 43 (2017) 15719–15728. doi:10.1016/j.ceramint.2017.08.133.

[50] B. Bracci, P. Torricelli, S. Panzavolta, E. Boanini, R. Giardino, A. Bigi, Effect of Mg2+, Sr2+, and Mn2+ on the chemico-physical and in vitro biological properties of calcium phosphate biomimetic coatings, J. Inorg. Biochem. 103 (2009) 1666–1674. doi:10.1016/j.jinorgbio.2009.09.009.

[51] C.F. Marques, A.C. Matos, I.A.C. Ribeiro, L.M. Gonçalves, A. Bettencourt, J.M.F. Ferreira, Insights on the properties of levofloxacin-adsorbed Sr- and Mg-doped calcium phosphate powders, J. Mater. Sci. Mater. Med. 27 (2016) 1–12. doi:10.1007/s10856-016-5733-2.

[52] M. Frasnelli, V.M. Sglavo, Effect of Mg2+doping on beta-alpha phase transition in tricalcium phosphate (TCP) bioceramics, Acta Biomater. 33 (2016) 283–289. doi:10.1016/j.actbio.2016.01.015.

[53] H. Ivankovic, G. Gallego Ferrer, E. Tkalcec, S. Orlic, M. Ivankovic, Preparation of highly porous hydroxyapatite from cuttlefish bone, J. Mater. Sci. Mater. Med. 20 (2009) 1039–1046. doi:10.1007/s10856-008-3674-0.

[54] X. Li, Y. Zhao, Y. Bing, Y. Li, N. Gan, Z. Guo, Z. Peng, Biotemplated Syntheses of Macroporous Materials for Bone Tissue Engineering Scaffolds and Experiments in Vitro and Vivo Biotemplated Syntheses of Macroporous Materials for Bone Tissue Engineering Sca ff olds and Experiments in Vitro and Vivo, ACS Appl. Mater. Interfaces. 5 (2013) 5557–5562. doi:10.1021/am400779e.

[55] P. Wang, L. Zhao, J. Liu, M.D. Weir, X. Zhou, H.H.K. Xu, Bone tissue engineering via nanostructured calcium phosphate biomaterials and stem cells, Bone Res. 2 (2014) 14017. doi:10.1038/boneres.2014.17.

[56] H. Ivankovic, E. Tkalcec, S. Orlic, G.G. Ferrer, Z. Schauperl, Hydroxyapatite formation from cuttlefish bones: kinetics, J. Mater. Sci. Mater. Med. 21 (2010) 2711–2722. doi:10.1007/s10856-010-4115-4.

[57] B.E.J. Denton, J. V Howarth, The osmotic mechanism of cuttlebone, J. Mar. Biol. Assoc. United Kingdom. 41 (1961) 351–363.

[58] K.M. Sherrard, Cuttlebone morphology limits habitat depth in eleven species of Sepia (Cephalopoda: Sepiidae), Biol. Bull. 198 (2000) 404–414. doi:10.2307/1542696.

[59] K. Farbod, M.R. Nejadnik, J.A. Jansen, S.C.G. Leeuwenburgh, Interactions Between Inorganic and Organic Phases in Bone Tissue as a Source of Inspiration for Design of Novel Nanocomposites, Tissue Eng. Part B Rev. 20 (2014) 173–188. doi:10.1089/ten.teb.2013.0221.

[60] L.-C. Gerhardt, A.R. Boccaccini, Bioactive glass and glass-ceramic scaffolds for bone tissue engineering, Materials (Basel). 3 (2010) 3867–3910. doi:10.1016/B978-1-84569-768-6.50005-3.

[61] T. Kokubo, H. Takadama, How useful is SBF in predicting in vivo bone bioactivity?, Biomaterials. 27 (2006) 2907–2915. doi:10.1016/j.biomaterials.2006.01.017.

[62] M. Tanahashi, T. Matsuda, Surface functional group dependence on apatite formation on self-assembled monolayers in a simulated body fluid, J. Biomed. Mater. Res. 34 (1997) 305–315. doi:10.1002/(SICI)1097-4636(19970305)34:3<305::AID-JBM5>3.0.CO;2-O.

**Table Captions**

**Table 1.** Quantitative analysis obtained by Rietveld refinement of the different CB derived compositions

**Table 2.** Planned and experimentally obtained molar concentrations of Sr, Mg and Zn in the BCP compositions.

**Table 3.** Porosities (%) of raw CB and of the uncoated and coated BCP scaffolds derived from CB with polymer solutions containing 5 (w/v %), expect for PLA in which the concentration was reduced to 3 (w/v %).

**Table 4.** Compressive strength (first row, MPa) and Young's modulus (second row, MPa) of raw CB and the uncoated and coated BCP scaffolds derived from CB.

**Table 1.** Quantitative analysis obtained by Rietveld refinement of the different CB derived compositions.

| Sample | Concentration of Sr, Mg and Zn (mol%) | | | | | |
|---|---|---|---|---|---|---|
| | Planned compositions | | | ICP elemental analysis | | |
| | Sr | Mg | Zn | Sr | Mg | Zn |
| BCP | 0 | 0 | 0 | 0.9 | 0.29 | 0.02 |
| BCP-6Sr | 6 | 0 | 0 | 2.6 | 0.32 | 0.02 |
| BCP-6Sr2Mg | 6 | 2 | 0 | 1.8 | 0.51 | 0.03 |
| BCP-6Sr2Zn | 6 | 0 | 2 | 1.8 | 0.31 | 0.80 |
| BCP-6Sr2Mg2Zn | 6 | 2 | 2 | 1.8 | 0.37 | 0.68 |

**Table 2.** Planned and experimentally obtained molar concentrations of Sr, Mg and Zn in the BCP compositions.

| Sample | wt.% of composition obtained by Rietveld refinement | |
|---|---|---|
| | HA | β-TCP |
| BCP | 47.75 | 52.25 |
| BCP-6Sr | 49.23 | 50.77 |
| BCP-6Sr2Mg | 29.45 | 70.55 |
| BCP-6Sr2Zn | 33.00 | 67.00 |
| BCP-6Sr2Mg2Zn | 47.85 | 52.15 |

**Table 3.** Porosities (%) of raw CB and of the CB-derived BCP scaffolds, uncoated and coated with polymer solutions containing 5 (w/v %), expect for PLA in which the concentration was reduced to 3 (w/v %).

| Polymer | Raw CB | BCP | BCP-6Sr | BCP-6Sr2Mg | BCP-6Sr2Zn | BCP-6Sr2Mg2Zn |
|---|---|---|---|---|---|---|
| – | 92.85±0.36 | 92.73±0.27 | 92.56±0.35 | 92.85±0.50 | 92.85±0.54 | 92.76±0.26 |
| PCL | – | 89.56±0.66 | 89.04±0.15 | 89.66±0.37 | 89.27±0.52 | 89.27±0.08 |
| PDLA* | – | 90.94±0.54 | 90.67±0.59 | 91.17±0.62 | 91.83±0.14 | 91.54±0.10 |
| PEA | – | 91.27±0.03 | 90.61±0.12 | 90.86±0.36 | 90.74±0.56 | 90.78±0.02 |
| PEU | – | 91.28±0.23 | 91.20±0.17 | 90.68±0.24 | 90.78±0.22 | 91.28±0.24 |

**Table 4.** Compressive strength (first row, MPa) and Young's modulus (second row, MPa) of the raw CB and the CB-derived BCP scaffolds uncoated and coated with polymer solutions containing 5 (w/v %), expect for PLA in which the concentration was reduced to 3 (w/v %).

| Polymer | Raw CB | BCP | BCP-6Sr | BCP-6Sr2Mg | BCP-6Sr2Zn | BCP-6Sr2Mg2Zn |
|---|---|---|---|---|---|---|
| – | 1.63±0.07 | 0.21±0.02 | 0.20±0.02 | 0.40±0.02 | 0.20±0.01 | 0.36±0.02 |
| – | 2.76±0.58 | 0.33±0.03 | 0.27±0.02 | 0.51±0.09 | 0.21±0.01 | 0.52±0.05 |
| PCL | – | 0.62±0.06 | 1.42±0.06 | 1.28±0.12 | 0.67±0.07 | 0.46±0.04 |
| | – | 1.22±0.24 | 2.10±0.29 | 2.22±0.31 | 1.29±0.08 | 0.66±0.05 |
| PDLA | – | 0.70±0.02 | 0.63±0.04 | 0.96±0.07 | 0.63±0.10 | 0.61±0.05 |
| | – | 1.26±0.16 | 0.98±0.16 | 1.35±0.17 | 1.01±0.22 | 1.01±0.13 |
| PEA | – | 0.31±0.05 | 0.36±0.02 | 0.30±0.03 | 0.25±0.04 | 0.20±0.01 |
| | – | 0.40±0.07 | 0.51±0.12 | 0.51±0.16 | 0.44±0.10 | 0.35±0.09 |
| PEU | – | 0.93±0.13 | 1.73±0.25 | 1.12±0.10 | 0.94±0.06 | 1.05±0.12 |
| | – | 1.31±0.23 | 2.61±1.01 | 1.57±0.20 | 1.59±0.23 | 1.54±0.18 |

**Figure Captions**

**Figure 1.** Thermal analysis of raw CB.

**Figure 2.** XRD patterns of BCP, BCP-6Sr, BCP-6Sr2Mg, BCP-6Sr2Zn and BCP-6Sr2Mg2Zn scaffolds sintered at 1200ºC. The diffraction pattern of β-TCP and HA standards, ICDD PDF 04-006-9376 and 04-015-7245, respectively, are also present for comparison purpose. Zoomed area within the 2θ range from 30-35º of the main HA and β-TCP peaks to show the effects of (a) $Sr^{2+}$, (b) $Sr^{2+}$ and $Mg^{2+}$, (c) $Sr^{2+}$ and $Zn^{2+}$ and (d) $Sr^{2+}$, $Mg^{2+}$ and $Zn^{2+}$ co-doping on the shift of the XRD peaks in comparison with undoped BCP.

**Figure 3.** FTIR spectra of BCP, BCP-6Sr, BCP-6Sr2Mg, BCP-6Sr2Zn and BCP-6Sr2Mg2Zn scaffolds (a) without polymer; and coated with (b) PCL; (c) PLA; (d) PEA; (e) PEU. The green and red lines correspond to the –PO4 and –OH groups, respectively. The blue lines correspond to the characteristic peaks of each polymer.

**Figure 4.** Microsctructure of raw CB. (a, b) μ-CT images highlighting the interconnectivity and sigmoidal path of the pillars; SEM micrographs (c) showing the presence of β-chitin and (d) the detail of the pillar wall.

**Figure 5.** SEM micrographs of the CB after HT transformation into BCP, BCP-6Sr, BCP-6Sr2Mg, BCP-6Sr2Zn and BCP-6Sr2Mg2Zn.

**Figure 6.** SEM micrographs of the coated CB derived scaffolds (BCP BCP-6Sr, BCP-6Sr2Mg, BCP-6Sr2Zn and BCP-6Sr2Mg2Zn) with the different polymers (PCL, PLA, PEA and PEU).

**Figure 7.** (a) SEM micrographs highlighting the interactions between the CB derived scaffolds and the different polymers. (b) Viscosity as a function of shear rate of the polymeric solutions.

**Figure 8.** Compressive strength of (a) raw CB and (b) the higher (BCP-6Sr2Mg, red line) and lower (BCP-6Sr2Zn, black line) obtained results after HT and sintering.

**Figure 9.** Representative result of the compressive strength of CB derived scaffolds after HT and coated with PCL, PLA, PEA or PEU: (A) BCP scaffolds; (b) BCP-6Sr scaffolds; (c) BCP-6Sr2Mg scaffolds; (d) BCP-6Sr2Zn scaffolds; (e) BCP-6Sr2Mg2Zn scaffolds.

**Figure 10.** SEM micrographs of the different coated CB after soaking in SBF solution for 14 days.

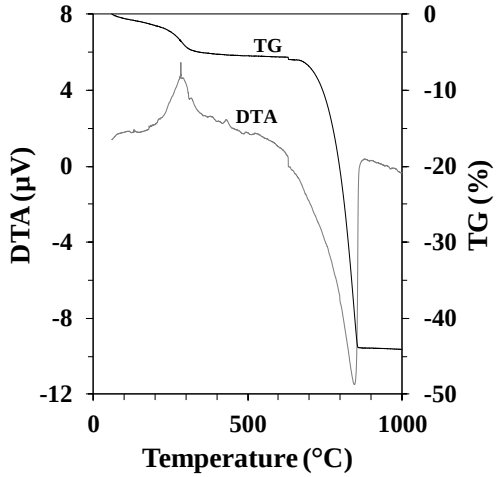


**Figure 1.** Thermal analysis of raw CB.

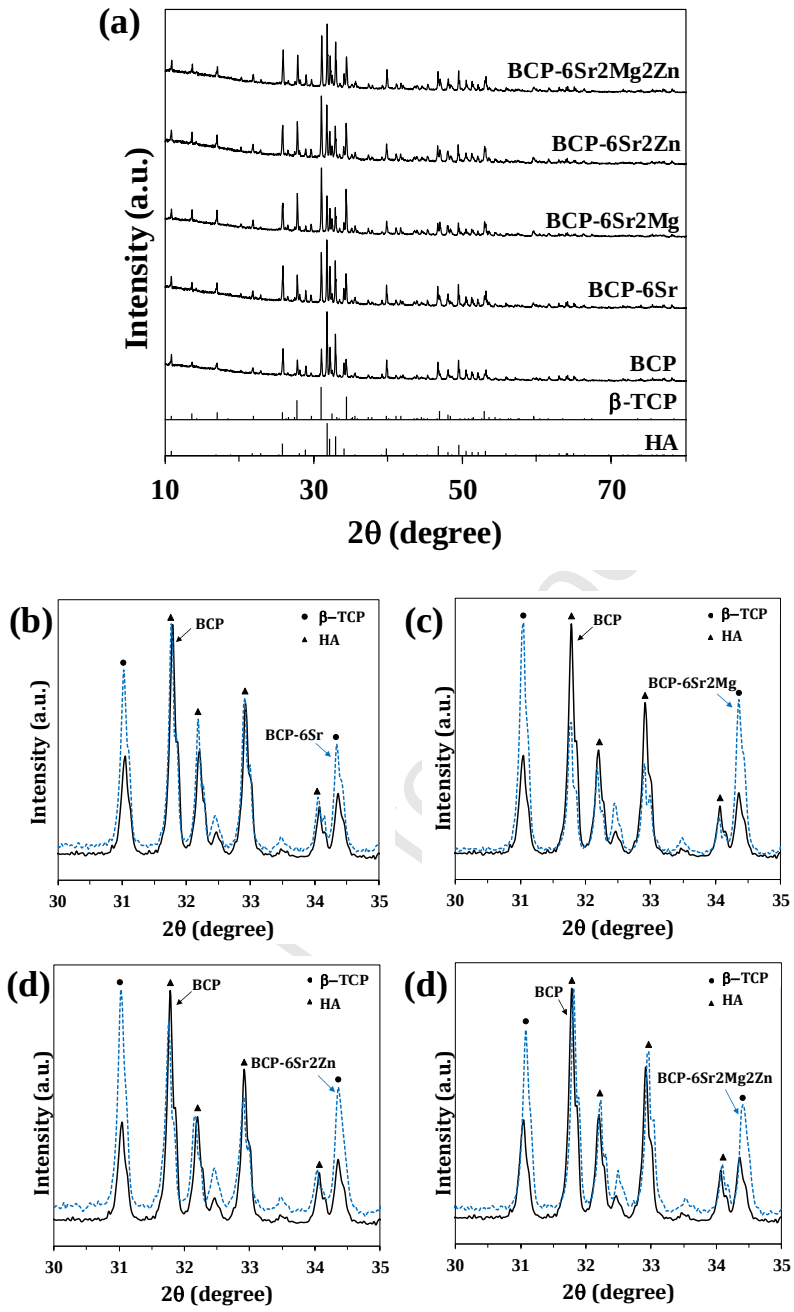


**Figure 2.** XRD patterns of BCP, BCP-6Sr, BCP-6Sr2Mg, BCP-6Sr2Zn and BCP-6Sr2Mg2Zn scaffolds sintered at 1200ºC. The diffraction pattern of β-TCP and HA standards, ICDD PDF 04-006-9376 and 04-015-7245, respectively, are also present for comparison purpose. Zoomed area within the 2θ range from 30-35º of the main HA and β-TCP peaks to show the effects of (a) $Sr^{2+}$, (b) $Sr^{2+}$ and $Mg^{2+}$, (c) $Sr^{2+}$ and $Zn^{2+}$ and (d) $Sr^{2+}$, $Mg^{2+}$ and $Zn^{2+}$ co-doping on the shift of the XRD peaks in comparison with undoped BCP.

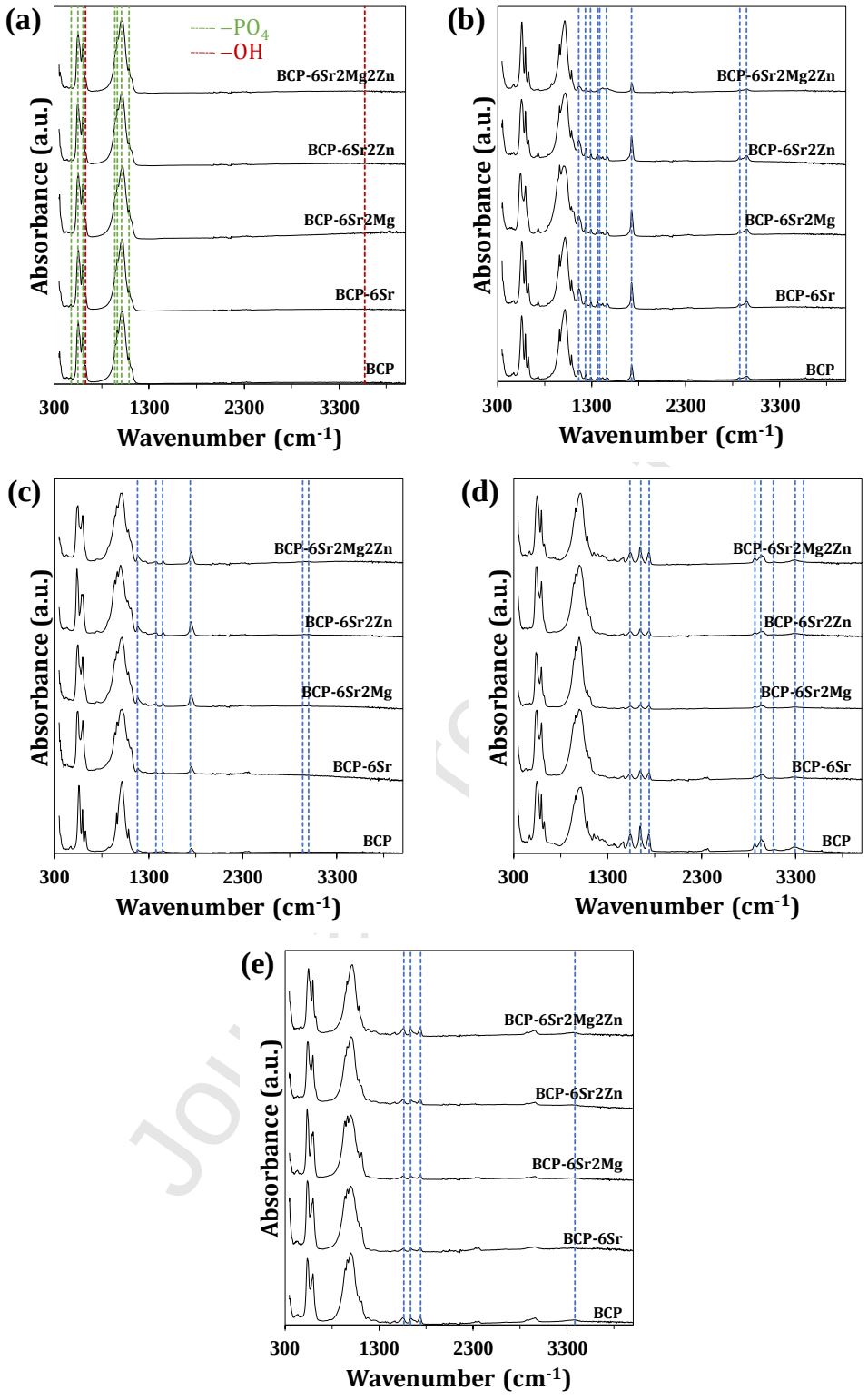


**Figure 3.** FTIR spectra of BCP, BCP-6Sr, BCP-6Sr2Mg, BCP-6Sr2Zn and BCP-6Sr2Mg2Zn scaffolds (a) without polymer; and coated with (b) PCL; (c) PLA; (d) PEA; (e) PEU. The green and red lines correspond to the –PO4 and –OH groups, respectively. The blue lines correspond to the characteristic peaks of each polymer.

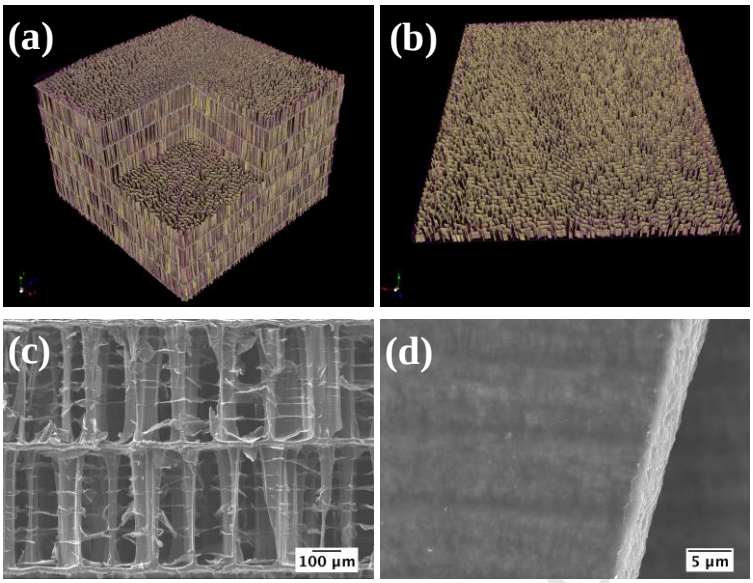


**Figure 4.** Microstructure of raw CB. (a, b) µ-CT images highlighting the interconnectivity and sigmoidal path of the pillars; SEM micrographs (c) showing the presence of β-chitin and (d) the detail of the pillar wall.

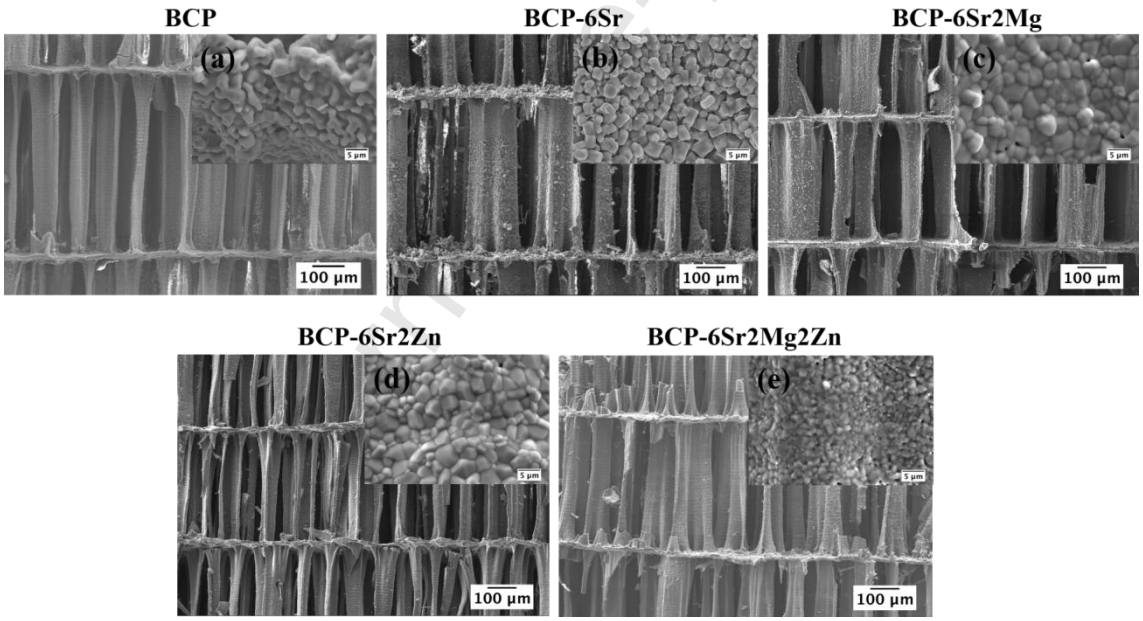


**Figure 5.** SEM micrographs of the CB after HT transformation into BCP, BCP-6Sr, BCP-6Sr2Mg, BCP-6Sr2Zn and BCP-6Sr2Mg2Zn. Zoomed SEM micrographs of the (a) BCP, (b) BCP-6Sr, (c) BCP-6Sr2Mg, (d) BCP-6Sr2Zn and (e) BCP-6Sr2Mg2Zn.

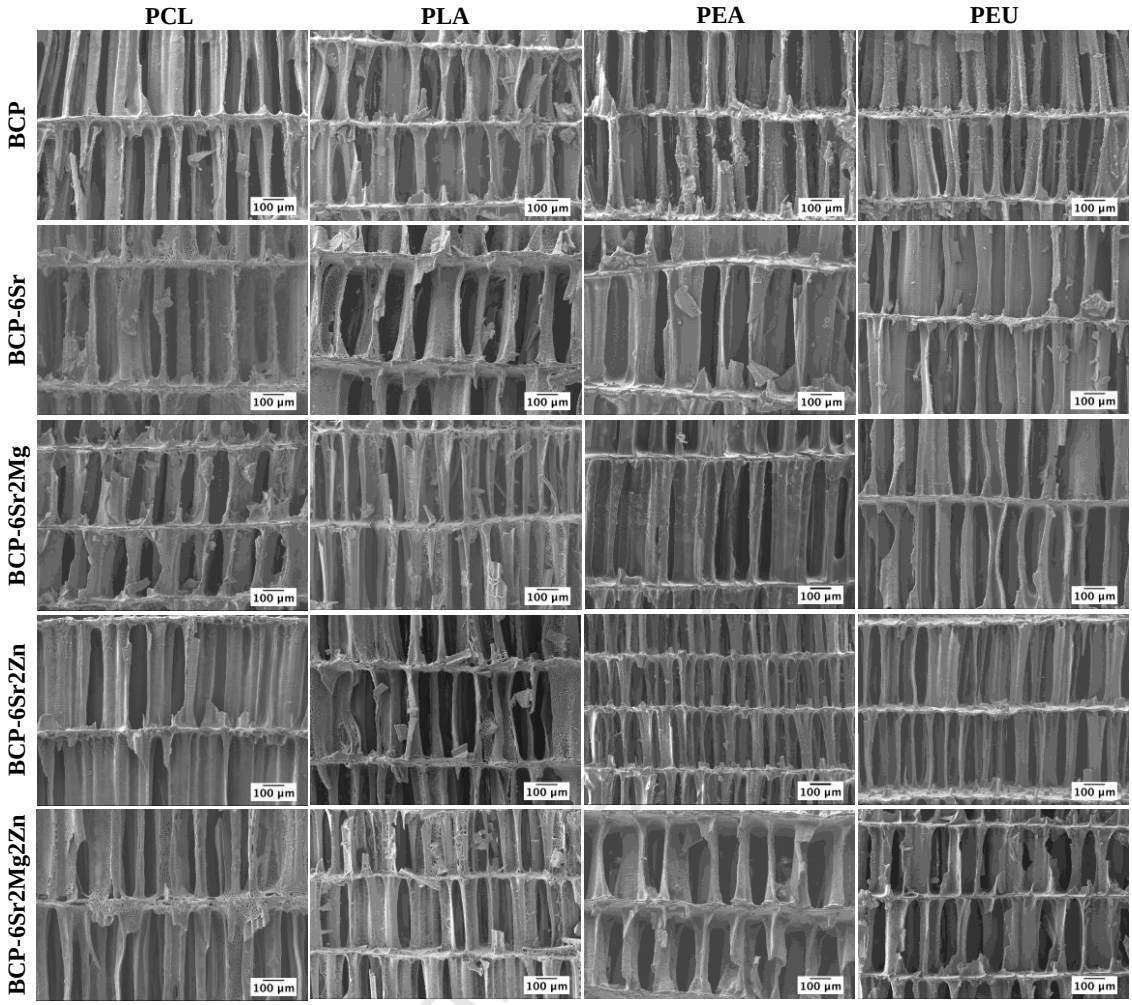


**Figure 6.** SEM micrographs of the coated CB derived scaffolds (BCP BCP-6Sr, BCP-6Sr2Mg, BCP-6Sr2Zn and BCP-6Sr2Mg2Zn) with the different polymers (PCL, PLA, PEA and PEU).

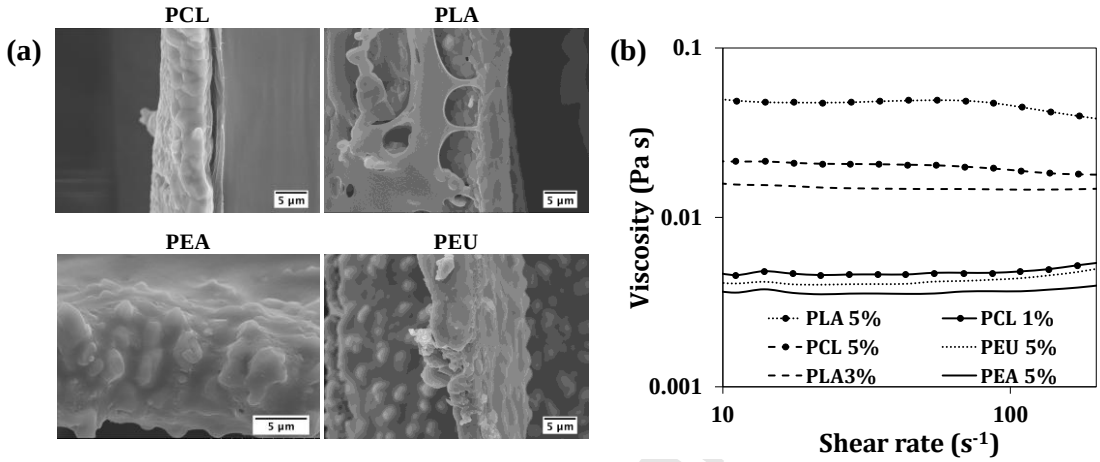


**Figure 7.** (a) SEM micrographs highlighting the interactions between the CB derived scaffolds and the different polymers. (b) Viscosity as a function of shear rate of the polymeric solutions.

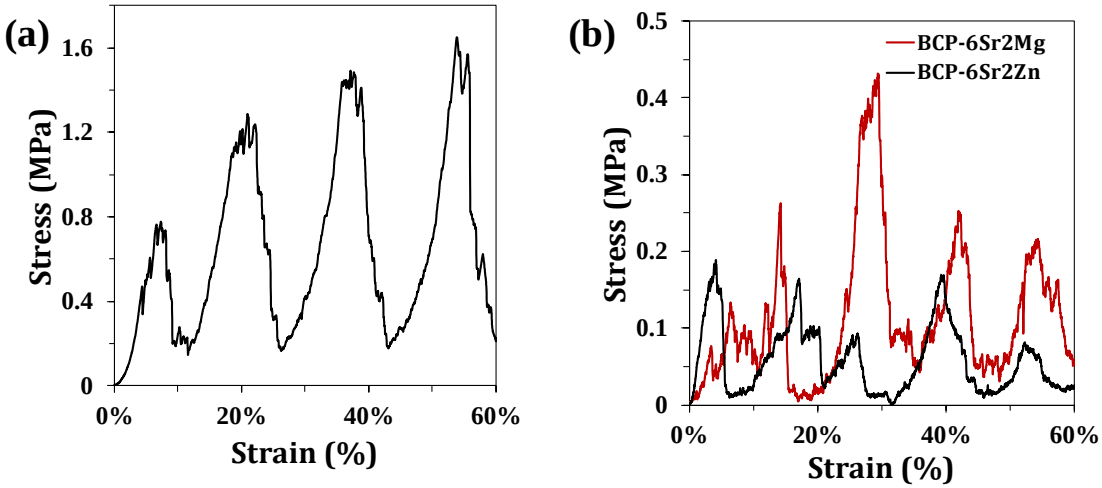


**Figure 8.** Compressive strength of (a) raw CB and (b) the higher (BCP-6Sr2Mg, red line) and lower (BCP-6Sr2Zn, black line) obtained results after HT and sintering.

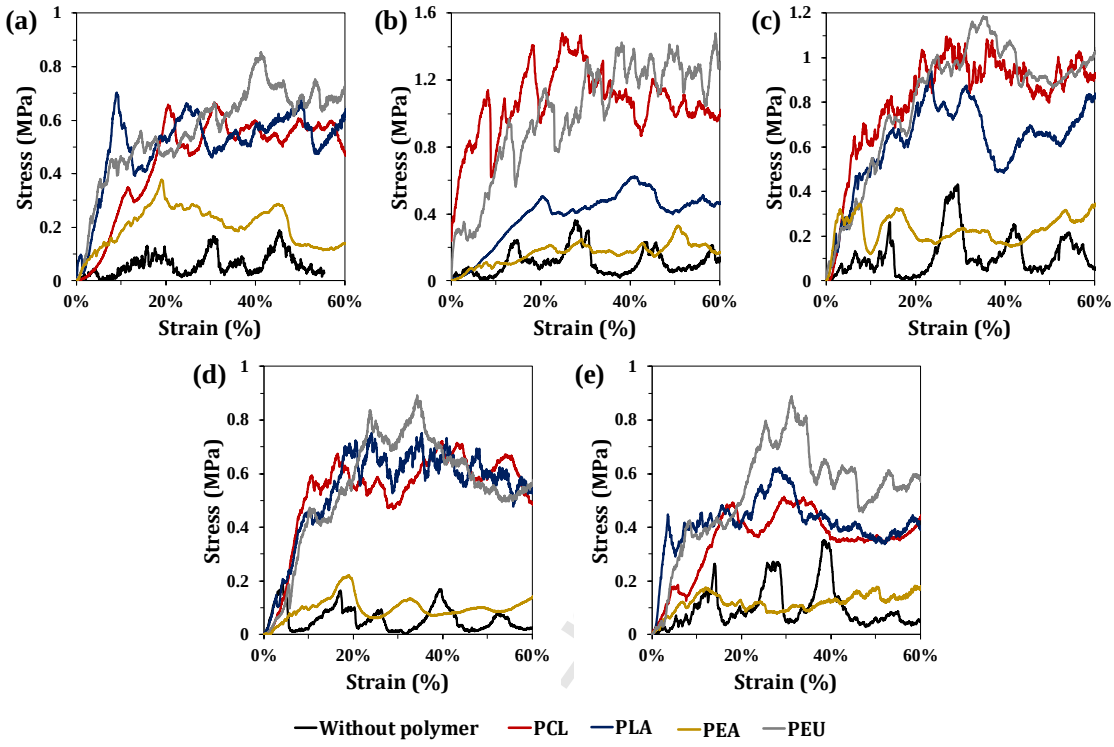


**Figure 9.** Representative result of the compressive strength of CB derived scaffolds after HT and coated with PCL, PLA, PEA or PEU: (A) BCP scaffolds; (b) BCP-6Sr scaffolds; (c) BCP-6Sr2Mg scaffolds; (d) BCP-6Sr2Zn scaffolds; (e) BCP-6Sr2Mg2Zn scaffolds.

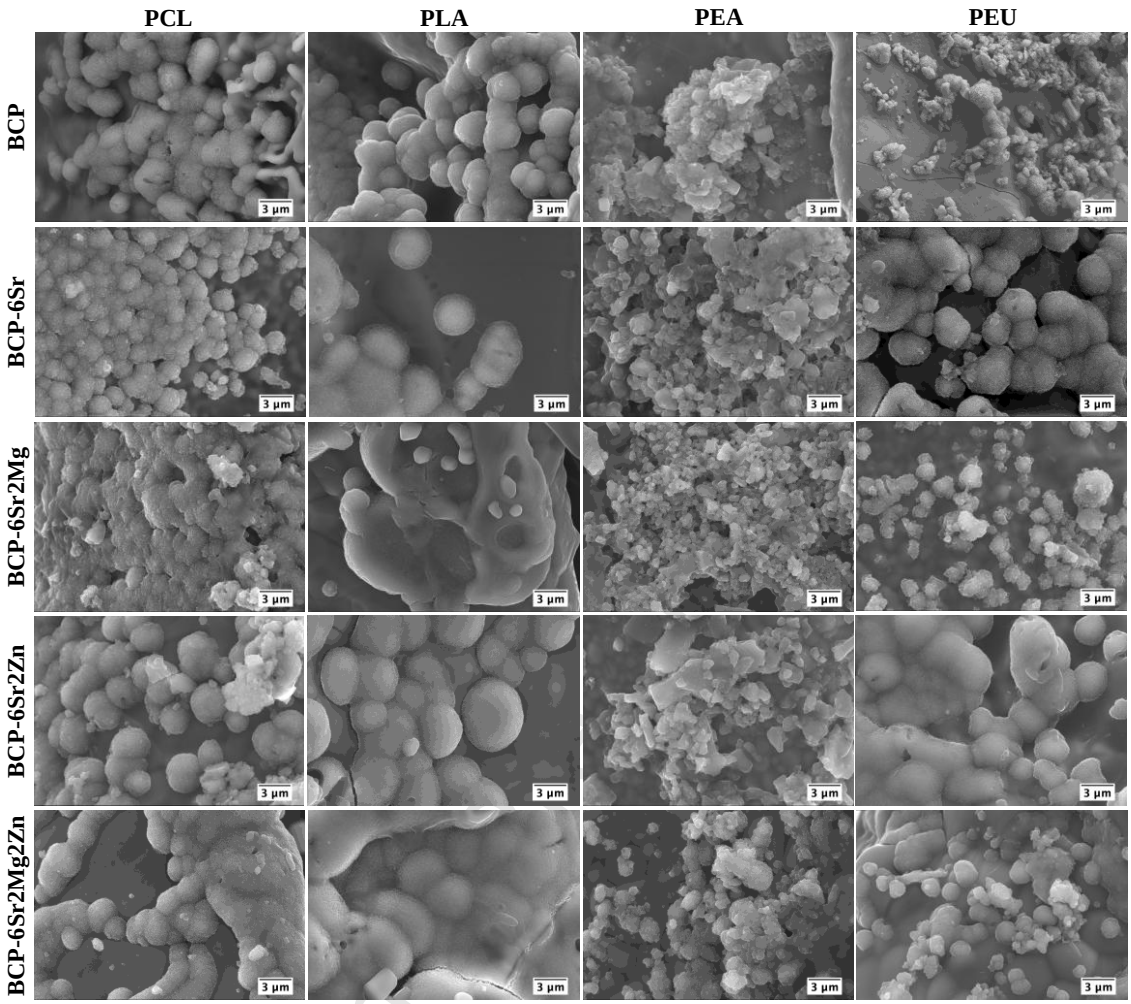


**Figure 10** SEM micrographs of the different coated CB after soaking in SBF solution for 14 days.

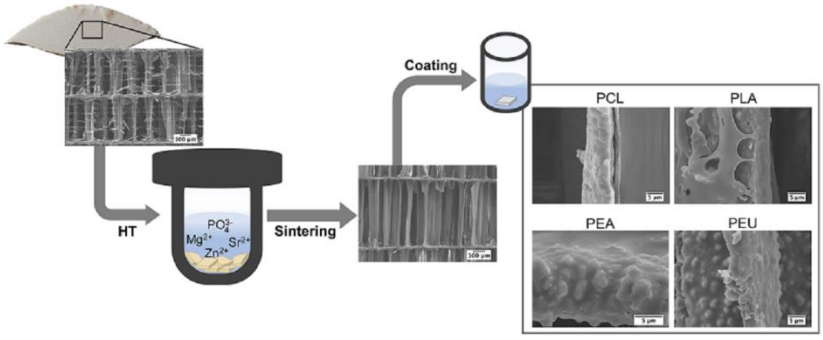


Graphical abstract

**Highlights**

- Full hydrothermal converting cuttlefish bones into doped biphasic calcium phosphates;
- Scaffolds with highly interconnected porous structure suitable for bone ingrowth;
- Synthesis of two new biopolymers, a poly(ester amide) and a poly(ester urea);
- Coating with biopolymers to reinforce mechanical properties of sintered scaffolds;
- New biopolymers offered > multi-functionalization efficacy than commercial ones.